Nanoscale

Cite this: *Nanoscale*, 2012, **4**, 2760

www.rsc.org/nanoscale

PAPER

Template synthesis of $SnO_2/\alpha\text{-}Fe_2O_3$ nanotube array for 3D lithium ion battery anode with large areal capacity

Weiqian Zeng,[a] Feipeng Zheng,[a] Ruizhi Li,[a] Yang Zhan,[a] Yuanyuan Li[b] and Jinping Liu*[a]

Received 11th January 2012, Accepted 20th February 2012
DOI: 10.1039/c2nr30089c

Electrodes with three-dimensional (3D) nanostructure are expected to improve the energy and power densities per footprint area of lithium ion microbatteries. Herein, we report a large-scale synthesis of a $SnO_2/\alpha\text{-}Fe_2O_3$ composite nanotube array on a stainless steel substrate *via* a ZnO nanowire array as an *in situ* sacrificial template without using any strong acid or alkali. Importantly, both SnO_2 and $\alpha\text{-}Fe_2O_3$ contribute to the lithium storage, and the hybridization of SnO_2 and $\alpha\text{-}Fe_2O_3$ into an integrated nanotube structure provides them with an elegant synergistic effect when participating in electrochemical reactions. Large areal capacities and good rate capability are demonstrated for such a composite nanotube array. Particularly noteworthy is that the areal capacities (*e.g.* 1.289 mAh cm^{-2} at a current rate of 0.1 mA cm^{-2}) are much larger than those of many previous thin-film/3D microbattery electrodes. Our work suggests the possibility of further improving the areal capacity/energy density of 3D microelectrodes by designing ordered hybrid nanostructure arrays.

Introduction

Rechargeable Li-ion batteries (LIBs) have attracted great interest in recent years due to their potential applications in modern portable electronic devices and plug-in hybrid electric vehicles (PHEVs).[1–3] They are also the vital power sources for a variety of electronic microsystems, such as computer memory chips, micromachines, microsensors, drug delivery systems and medical implant devices.[1] Nevertheless, in contrast to the recent advancements in these microdevices, reduction of battery size has not kept pace with the size reduction of electronic devices, partly due to the difference in the level of research activity and the difficulty in the manipulation of the small area of the electrode structure. Hence, future efforts should be made to develop smaller micro-/nanobatteries with the largest capacity per footprint area possible.[4] Insufficient power and energy from state-of-the-art two-dimensional (2D) microbattery configurations lead to the search for the development of a 3D micro-/nanobattery using cheap and abundant electrode materials.[3–5] As compared to 2D thin film structure, 3D structures such as nanowire/nanotube arrays can potentially utilize the vertical dimension to increase the active material loading (thus the areal capacity) while maintaining similar Li ion-transport distances. In addition, it generally provides a larger surface area to enhance the interfacial kinetics, sufficient space to accommodate the stress relaxation and a direct pathway for electron transport.[6]

Nanostructured metal oxides, such as $\alpha\text{-}Fe_2O_3$ and SnO_2, have long been considered as superior materials to graphite for lithium storage because of their higher specific capacities (500–1000 mAh g^{-1}) and improved safety.[2,7–10] A major drawback of tin- and iron-based electrodes is the giant volume expansion/contraction upon lithium insertion/deinsertion that leads to cracks within electrode films with the subsequent electrical isolation and loss of electrochemical activity. A large number of studies have focused on the improvement of the reversible capacity and cyclability of $\alpha\text{-}Fe_2O_3$ and SnO_2 by fabricating them into delicate nanostructures (nanotubes,[2] nanowires/rods,[8,9] and branched nanostructures,[11] *etc.*[12,13]) with short lithium diffusion paths and large surface area. In particular, nanotubes have gained much more attention due to their hollow structure, which can provide sufficient space for electrolyte accommodation, making both the inner and outer tube walls fully exposed to lithium ions. Despite much progress on using these smart nanostructures in conventional large-volume LIBs, there are very few reports on their rechargeable microbattery application[14,15] and to the best of our knowledge, there is no report concerning 3D microbatteries based on $SnO_2/\alpha\text{-}Fe_2O_3$ composite nanotube electrodes.

In this paper, we report a facile route to fabricate a $SnO_2/\alpha\text{-}Fe_2O_3$ composite nanotube array for the anode material of LIBs using ZnO nanowires that are grown directly on a conductive stainless steel substrate as the sacrificial template. Interestingly, during the introduction of $\alpha\text{-}Fe_2O_3$ into the composite, the ZnO template can be dissolved *in situ* in the absence of any strong acid or alkali, which not only simplifies the operation but is also safe and environmentally-friendly. When used as a 3D microbattery anode, it is proved by a set of electrochemical experiments that

---

[a] *Institute of Nanoscience and Nanotechnology, Department of Physics, Central China Normal University, Wuhan, 430079, P. R. China. E-mail: liujp@phy.ccnu.edu.cn*
[b] *Department of Electronic Science and Technology, Huazhong University of Science and Technology, Wuhan, 430074, P. R. China*

the as-grown SnO_2/α-Fe_2O_3 nanotube array electrode exhibits good electrochemical performance in terms of areal capacity, cyclability and rate capability, due to the synergistic effect between these two components in an integrated structure. In particular, the areal capacities are much higher than many previous values of thin-film and 3D battery electrodes, including Si film-based Li-ion microbattery anode. The present work reveals the great potential of metal oxide composite nanotube arrays in the application for future 3D micro-/nanobatteries.

Experimental section

Our experiment contains two steps: the growth of a ZnO–SnO_2 core-shell nanowire array and the fabrication of a SnO_2/α-Fe_2O_3 composite nanotube array. The general process is illustrated in Scheme 1 in detail. For the synthesis of ZnO–SnO_2 core-shell nanowires, two aqueous solutions containing 0.033 g of $K_2SnO_3 \cdot 3H_2O$ and 0.333 g of urea were firstly prepared and mixed with vigorous stirring. Distilled water was then added to obtain a final volume of 70 mL. With a stainless steel foil covered with a pristine ZnO nanowire array (prepared as described elsewhere[16]) placed on the bottom, the above mixture was transferred into a Teflon®-lined stainless-steel autoclave and hydrothermally treated at 90 °C for 2 h. After the reaction was finished, the foil was taken out and ultrasonicated for 7 s and then rinsed several times with distilled water to remove any possible impurities. To synthesize the SnO_2/α-Fe_2O_3 composite nanotube array, the foil-supported ZnO–SnO_2 core-shell nanowire array was immersed into an aqueous Fe^{3+} solution (0.0025 g $Fe(NO_3)_3 \cdot 9H_2O$ mL^{-1}) for 2.25 h. After this, the foil substrate was taken out, dried at 60 °C, and further annealed at 500 °C in Ar gas for 2 h. It should be pointed out that our synthesis avoided the use of strong acids (such as HCl) for the ZnO template removal, making it more environmentally friendly and easier to be manipulated.

Products were characterized using powder X-ray diffraction (XRD)(Bruker D-8 Avance), transmission electron microscopy (TEM) (JEM-2010FEF, 200kV) and scanning electron microscopy (SEM) (JSM-6700F, 5.0kV). The Swagelok-type battery was assembled in an Ar-filled glove box (Mbraun, Unilab, Germany) by directly using the SnO_2/α-Fe_2O_3 array (~1 mg) on stainless steel foil as the anode (the array on one side of the foil was removed for electrical contacting), Li metal circular foil (0.59 mm thick, 14 mm diameter) was used as the counter and reference electrodes, a microporous polypropylene membrane as the separator, and 1 M solution of $LiPF_6$ in ethylene carbonate (EC) and diethyl carbonate (DEC)(1 : 1 by volume) as the electrolyte. The cells were aged for 12 h before measurement. The charge–discharge cycling was performed at room temperature by using a multichannel battery tester (model SCN, USA). Areal capacity values were calculated based on the area of the working electrode.

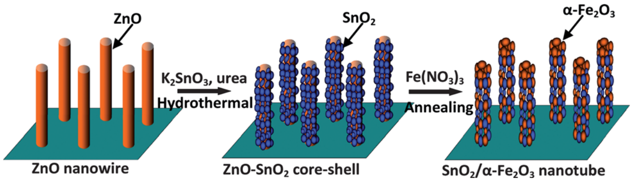

Scheme 1 Schematic illustration of the fabrication process of the composite nanotube array electrode.

Results and discussion

Fig. 1a shows the typical SEM image of an aligned ZnO nanowire array synthesized based on the protocol reported elsewhere.[16,17] It can be seen that there is sufficient space between neighboring nanowires, which can allow molecules to easily adsorb onto the nanowire surface. After a 2 h hydrothermal reaction (the first step in Scheme 1), the ZnO nanowires are obviously coated by a uniform layer of the nanostructured shell (Fig. 1b). The shell is constructed by many tiny SnO_2 particles, leading to the formation of porous walls. The generation of SnO_2 is based on the following reaction: $CO(NH_2)_2 + SnO_3^{2-} + H_2O \rightarrow SnO_2 + CO_3^{2-} + 2NH_3$, which has been dramatically promoted under hydrothermal conditions. Moreover, as shown in the magnified pictures in Fig. 1c and the inset of Fig. 1b, gaps generally appear between the ZnO nanowire and SnO_2 nanoshell. This is presumably due to partial dissolution of ZnO in self-generated alkali conditions during the SnO_2 deposition. Based on Fig. 1c, the thickness of the SnO_2 shell is estimated to be ~30 nm. Along with SEM observations, the XRD patterns shown in Fig. 1d clearly demonstrate the composition evolution. For the core-shell array sample, in addition to the peaks from ZnO and stainless steel substrate, other peaks at 33.82° *etc.* can be well indexed to tetragonal rutile SnO_2 (JCPDS card No. 41-1445).

The construction of the SnO_2/α-Fe_2O_3 composite nanotube array was achieved by immersing a ZnO–SnO_2 core-shell array directly in Fe^{3+} aqueous solution followed by annealing treatment (the second step in Scheme 1). During the 2.25 h immersion, Fe^{3+} started to hydrolyze, resulting in the formation of the $Fe(OH)_3$ colloid and protons (H^+) ($Fe^{3+} + 3H_2O \rightarrow Fe(OH)_3 + 3H^+$). It's reasonable to speculate that the ions can easily diffuse through SnO_2 to the ZnO surface due to the porous structure of the SnO_2 layer. Furthermore, those gaps between the ZnO

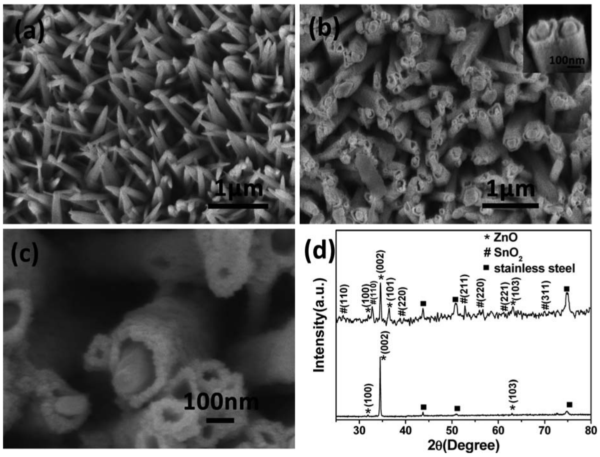

Fig. 1 SEM images of (a) ZnO nanowire array, (b, c) ZnO–SnO_2 core-shell nanowire array. Inset in Fig. 1b is the enlarged picture of two core-shell nanowires, showing the gaps between core and shell. (d) XRD patterns of pure ZnO and the core-shell nanowire arrays.

nanowire core and SnO_2 shell observed in SEM (Fig. 1b) could also allow Fe^{3+} ions to enter freely. As a result, the space from the surface of the SnO_2 shell to that of the ZnO nanowire was sufficiently saturated by Fe^{3+}. In the vicinity of the core-shell array, the H^+ ions from *in situ* hydrolysis etched ZnO, and the consumption of H^+ accelerated the hydrolysis reaction simultaneously, leading to a reinforced and heterogeneous deposition of $Fe(OH)_3$. Intensive hydrolysis and ZnO dissolution was mutually promoted,[18] eventually giving rise to the SnO_2-$Fe(OH)_3$ tubular array (Fig. 2a). After further annealing, the $Fe(OH)_3$ colloid was readily converted into α-Fe_2O_3 and the SnO_2/α-Fe_2O_3 composite nanotube array was attained accordingly (Fig. 2b–e), which maintained a similar array orientation to the initial ZnO array. Fig. 2c shows the magnified image of the SnO_2/α-Fe_2O_3 composite nanotubes and illustrates that the diameter is about 200–400 nm. Comparing Fig. 2b–e with Fig. 1b and c, the obvious increase of diameter and the distinct change of surface topography (increased roughness) are likely to prove the composition variation. Further observations in Fig. 2d and 2e represent the close-up pictures of some individual nanotubes with open ends. In Fig. 2d, a special mention should be made to the fact that the hexagonal shape of the inner wall results from the traditional hexagonal contour of the ZnO nanowire template, which further confirms the templating mechanism in this process. The XRD pattern shown in Fig. 2f confirms the composition of the composite nanotubes. Apart from peaks from the substrate, other peaks successfully confirm the presence of α-Fe_2O_3 (JCPDS Card No.33-0664) with SnO_2 and no apparent peaks from ZnO can be detected, affirming the removal of single-crystal ZnO sacrificial template.

The structure and morphology evolution of the composite array was further investigated by TEM. Fig. 3a and its inset display a TEM image of a single ZnO–SnO_2 core-shell nanowire. A porous layer of SnO_2 is observed on the ZnO nanowire surface, some of which have already been etched at this growth stage, in good agreement with SEM observation. The high-resolution TEM (HRTEM) image in Fig. 3b demonstrates that the SnO_2 shell is in fact composed of many interconnected tiny nanocrystals. The clear lattice spacing of *ca.* 0.273 nm corresponds to the interplanar distance of the (101) plane of rutile SnO_2. To further verify the composition of the core-shell nanowire, the nanowire was analyzed by energy-dispersive X-ray spectroscopy (EDS) at two different positions (A: outer shell; B: inner core-shell nanowire) (Fig. 3c). Note that the carbon and Cu signals are from the carbon-supported Cu grid. As expected, while the outer shell contains only Sn and O, the inner core-shell wire also contains Zn in addition to Sn and O. Fig. 3d shows a typical TEM image of two SnO_2/α-Fe_2O_3 composite nanotubes, whose outside surface is magnified in Fig. 3e. In the TEM, the tubular structure can be unambiguously identified. The tube wall also consists of numerous nanoparticles; the thickness of the tube wall is determined to be ~100 nm (see black arrows). HRTEM images (right part of Fig. 3e) reveal that the later deposited particles are also single-crystalline with interplanar spacings of about 0.36, 0.27 and 0.25 nm, respectively, consistent with the standard values for (012), (104) and (110) planes of α-Fe_2O_3. Two distinct spots (C: body of the tube; D: mouth of the tube) were examined by EDS (Fig. 3f). While the body of the tube contains Fe, Sn and O, the mouth of the tube is relatively lacking in Sn, which is reasonably assumed to be caused by the absence of a SnO_2 cap in the initial ZnO–SnO_2 core-shell nanowires and subsequently a great amount of deposition of ferric compounds during the immersion period. EDS results clearly demonstrate that SnO_2 and α-Fe_2O_3 have been incorporated into an integrated nanotube structure.

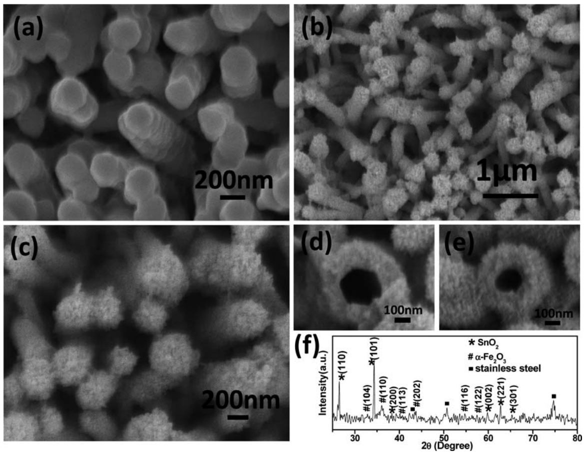

Fig. 2 SEM images of (a) SnO_2–$Fe(OH)_3$ tubular array, (b, c) SnO_2/α-Fe_2O_3 composite nanotube array, (d, e) two individual nanotubes with open tips. (f) XRD pattern of the composite array.

In virtue of the robust mechanical adhesion and good electrical contact enabled by the direct growth of metal oxide nanostructures on the current collector, the SnO_2/α-Fe_2O_3 composite nanotube array was further tested as a lithium ion battery anode. The electrochemical experiments were conducted in a two-electrode configuration with the as-prepared array on the stainless steel substrate used directly as the working electrode and Li foil as the counter electrode. The electrochemical reaction mechanism of Li with SnO_2 and α-Fe_2O_3 has been well studied and can be expressed in the following equations.[10,19–22]

$$SnO_2 + 4Li^+ + 4e^- \rightarrow Sn + 2Li_2O \qquad (1)$$

$$xLi^+ + xe^- + Sn \leftrightarrow Li_xSn (0 \le x \le 4.4) \qquad (2)$$

$$\alpha\text{-}Fe_2O_3 + 6Li^+ + 6e^- \leftrightarrow 2Fe + 3Li_2O \qquad (3)$$

To obtain the charge and discharge profiles, the assembled cell was firstly tested at a constant current density of 0.1 mA cm^{-2} (~132.7 mA g^{-1}) with a potential range between 5 mV and 2.5 V. The results of the first three cycles are shown in Fig. 4a. The first real discharge capacity is estimated to be as high as 1.289 mAh cm^{-2}, whereas, the corresponding charge capacity is approximately 0.839 mAh cm^{-2}, revealing a Coulombic efficiency of 65%, which is comparable to the previous report of SnO_2 nanotube arrays[10] (~61%) and much higher than that of the SnO_2 nanowire arrays (~56%[23] and ~58%[20]). Considering that the reaction of α-Fe_2O_3 with Li is electrochemically reversible,[11,24] the irreversible reaction of eqn (1) and the formation of solid-electrolyte interphase (SEI) film are responsible for the irreversible capacity loss during the first charge–discharge cycle.[9] In the second and third cycles, the discharge capacity decreases gradually to 0.982 and 0.900 mAh cm^{-2}, respectively. The charge

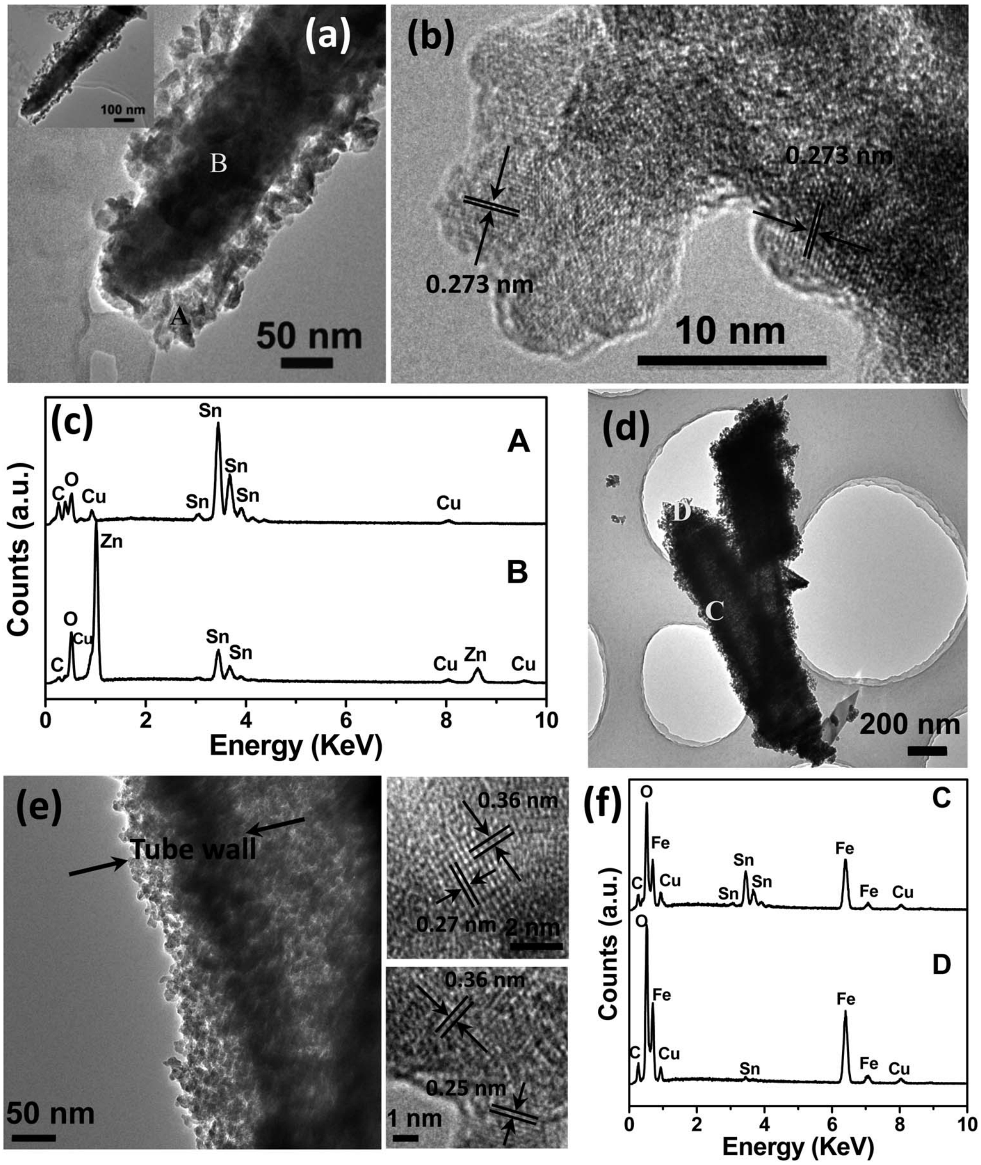

Fig. 3 (a) TEM image of a single ZnO–SnO_2 core-shell nanowire. Inset is a low-magnification image. (b) HRTEM image of the shell. (c) EDS results recorded from spots A and B in Fig. 3a. (d, e) TEM image of two individual $SnO_2/\alpha\text{-}Fe_2O_3$ nanotubes. Right part in Fig. 3e shows the HRETM images of the tube wall. (f) EDS spectra recorded from positions C and D in Fig. 3d.

capacity, however, has similar values around 0.811 mAh cm^{-2}. The charge–discharge profiles of the composite tube array should have contributions from both SnO_2 and $\alpha\text{-}Fe_2O_3$. Electrochemical behaviors and features of these two active materials[9,24] are properly reflected in Fig. 4a. The long plateau of the first discharge curve between 0.6 and 1.25 V can be ascribed to the decomposition of SnO_2 to Sn and Li_2O (eqn (1)) and the formation of cubic $Li_2Fe_2O_3$ (the first step of Li insertion into $\alpha\text{-}Fe_2O_3$). The plot with the potential below 0.6 V corresponds to the alloying reaction between Sn and Li (forward reaction in eqn (2)) and the reduction from Fe^{2+} to Fe^0 with the formation of amorphous Li_2O.[18,19,23,25,26] The above results can be further verified by the differential capacity *versus* voltage plot, as shown in Fig. 4b, with three main peaks centered at ~1.0, ~0.73 and ~0.24 V respectively during the discharge process. The remaining small peak at ~0.45 V in the same process is probably due to the irreversible decomposition reaction of electrolyte.[19,26] Meanwhile, during the charge process, two broad peaks centered at ~0.5 and ~1.65 V are also observed, corresponding to the dealloying of Li_xSn and reversible oxidation of Fe^0 to Fe^{3+}, respectively.[27]

The rate capability was further tested for the $SnO_2/\alpha\text{-}Fe_2O_3$ composite nanotube array electrode, which is of significant importance for high-power energy storage.[17,28] The first charge–discharge curves at different current densities of 0.2, 0.25, 0.3, 0.4, 0.6 mA cm^{-2} were recorded, as revealed in Fig. 4c. The charge capacities at these rates are 0.675, 0.572, 0.433, 0.388, 0.293 mAh cm^{-2}, while the discharge capacities are 1.144, 0.949, 0.744, 0.634, 0.507 mAh cm^{-2}, respectively. The discharge capacity per unit weight (1518 mAh g^{-1}) at 0.2 mA cm^{-2} (265.4 mA g^{-1}) is comparable to that of previous SnO_2 nanotube arrays (~1600 mAh g^{-1} at 200 mA g^{-1}).[10] Fig. 4d displays the first

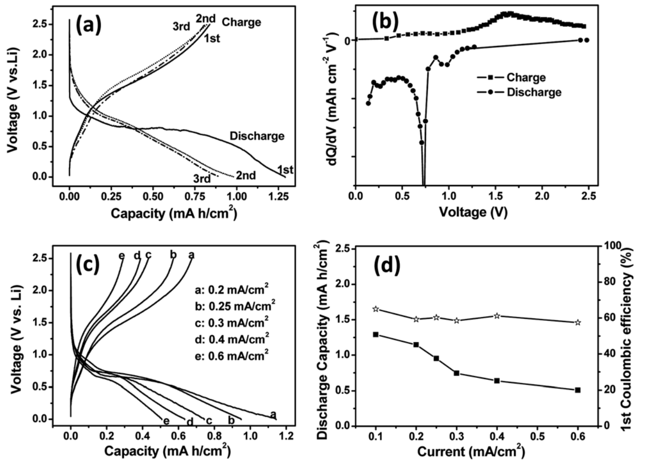

Fig. 4 (a) Charge–discharge profiles of the $SnO_2/\alpha\text{-}Fe_2O_3$ composite nanotube array for the first three cycles. (b) The 1st-cycle differential capacity *versus* voltage plots. (c) Rate performance of $SnO_2/\alpha\text{-}Fe_2O_3$ array. d) Discharge capacity and the 1st Coulombic efficiency of the composite array *versus* current density plots. The current density ranges from 0.1 to 0.6 mA cm^{-2}.

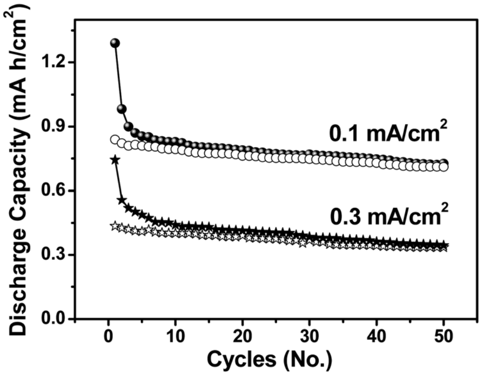

Fig. 5 Cycling stability of $SnO_2/\alpha\text{-}Fe_2O_3$ composite nanotube array.

Coulumbic efficiency of the electrode and the discharge capacity of the first cycle under different current densities varies from 0.1 to 0.6 mA cm^{-2}. The result indicates that when the current is gradually increased to 0.6 mA cm^{-2}, the Coulombic efficiencies stabilize at around 60%. At 0.4 mA cm^{-2}, for example, the electrode exhibits charge and discharge capacities of 0.388 and 0.634 mAh cm^{-2}, and the corresponding Coulombic efficiency is over 61%. Additionally, the discharge capacity can be retained at around 0.51 mAh cm^{-2} as the current density increases to 5 times of the initial one to 0.6 mA cm^{-2}, which is somewhat superior to that of many previous reports.[4a,5,29,30] The rate performance of electrodes are greatly determined by the microstructure of the active materials when the components are confirmed. In our case, the $SnO_2/\alpha\text{-}Fe_2O_3$ composite is constructed in the form of porous nanotube arrays. On one hand, the porous nature of the tube wall facilities the diffusion of Li ions while also providing large surface area reaction sites. The hollow structure of nanotubes helps to enlarge the space for electrolyte storage, with which lithium ions can insert into both inner and outer tube walls more easily and freely. On the other hand, the ordered architecture ensures the direct pathway for electron transport from/to the current collector. Both of these together can lead to enhanced interfacial kinetics, which meets the key requirement for quick charge and discharge.

What's more, the cyclability test was carried out to demonstrate the advantages of a $SnO_2/\alpha\text{-}Fe_2O_3$ composite nanotube array electrode at the current densities of both 0.1 and 0.3 mA cm^{-2}. The charge–discharge cycling was tested for up to 50 cycles, and the result is displayed in Fig. 5. It is evident that although the areal capacity decreases sharply during the first three cycles, the electrode still shows a high discharge capacity of 0.727 mAh cm^{-2} after 50 cycles at a current density of 0.1 mA cm^{-2}, maintaining ~56% of the first cycle. This cycling property is better than that of the SnO_2 nanotube array anode reported recently[10] (after 20 cycles retains ~50%). The charge capacity retention (84.7% after 50 cycles) is also higher than that of the $\alpha\text{-}Fe_2O_3$ nanotube array (~78%).[18] In addition, at ~0.1 mA cm^{-2} (~132.7 mA g^{-1}), our composite nanotube array electrode demonstrated higher capacity per unit weight (~965 mAh g^{-1}) than the pure $\alpha\text{-}Fe_2O_3$ nanotube array (~700 mAh g^{-1})[18] after 50 cycles. The Coulombic efficiencies for the first three cycles are about 65%, 83%, 90% respectively, while those of the other cycles stay steadily at more than 95%, which is comparable to the previous reports.[10,20,24] When the current density increases twice to 0.3 mA cm^{-2}, the array electrode demonstrated similar cycling stability. The areal discharge capacity after 50 cycles is still maintained over 0.344 mAh cm^{-2} and ~50% of the first discharge capacity is retained.

To the best of our knowledge, the areal capacity displayed here is much higher than many previous reports, such as TiO_2 nanotubes[31] (first discharge capacity is 0.678 mAh cm^{-2} and decreases to 0.2 mAh cm^{-2} after 45 cycles at current density of 0.025 mA cm^{-2}), Fe_3O_4 thin film[30] (0.3 mAh cm^{-2} at 0.01 mA cm^{-2}), crystalline SnO_2 nanowire/TiO_2 nanotube[15] (0.14 mAh cm^{-2} at 0.05 mA cm^{-2}), Si columnar thin film[5] (0.09 mAh cm^{-2} at 0.012 mA cm^{-2}), and a carbon micro-net film[29] (0.15 mAh cm^{-2} at 0.006 mA cm^{-2}). Typically, the current densities in our experiment are much larger, but the areal capacities and cyclability of our $SnO_2/\alpha\text{-}Fe_2O_3$ composite nanotube arrays are much better.

The reason for the performance improvement (larger areal capacity, better rate capability and cycling stability, *etc.*) can be ascribed to the elegant combination of SnO_2 and $\alpha\text{-}Fe_2O_3$, two promising LIB anode materials, into an integrated tubular architecture. Compared with a 2D thin film structure, the extra dimension of a 3D nanotube array can be of vital help to increase the active material loading while maintaining similar Li ion-transport efficiency, which is beneficial to the enhancement of areal capacity. This was realized by the templating method, using inexpensive ZnO nanowires in our case. Moreover, the synergistic effect between SnO_2 and $\alpha\text{-}Fe_2O_3$ is of great importance. In each nanotube, SnO_2 nanoparticles are dispersed with $\alpha\text{-}Fe_2O_3$ around them. As revealed in the charge–discharge profiles, alloying and dealloying is the dominant process contributing to lithium storage and delivery for SnO_2 after the first cycle, which occurs at a lower potential as compared to the electrochemical reaction of $\alpha\text{-}Fe_2O_3$ with Li. As a result, when SnO_2 nanoparticles are electrochemically engaged, Fe_2O_3 nanoparticles are almost inactive and can function as a buffering matrix to alleviate the huge strain stress during the alloying and dealloying process, as well as a block to prevent against generated Sn aggregating. Similarly, at high potential, SnO_2 (Sn particles and Li_2O formed after the first cycle) can also help to buffer the volume change of Fe_2O_3. This kind of mutual interaction would be essential to maintain a high areal capacity even after tens of cycles. In addition, it has been reported that the transition metal Fe produced by the conversion reaction (forward reaction of eqn (3)) has a catalytic function to promote the backwards reaction of eqn (1),[11,32] which should be responsible for the observed larger Coulombic efficiency.

Conclusions

In summary, starting with a ZnO nanowire array as the sacrificial template, we have successfully fabricated a SnO_2/α-Fe_2O_3 composite nanotube array on the current collector substrate. The electrochemical performance of such a hybrid array as a binder- and additive-free electrode for LIBs was systematically investigated. The results indicated that the array electrode has a large areal capacity, good rate capability and high Coulombic efficiency. The comprehensive electrochemical property is much better than many of the previously reported thin-film and 3D nanostructured anodes, which could be attributed to a synergistic effect between SnO_2 and α-Fe_2O_3 as well as the porous and ordered nanotubes that provide increased electrochemical reaction kinetics. Moreover, such a strategy can be readily extended to synthesize other metal oxide composite nanotube array electrodes, which have potential applications in small-scale energy storage devices such as microbatteries and micro-supercapacitors.

Acknowledgements

The work was supported by grants from the National Natural Science Foundation of China (No. 51102105, 11104088) and Natural Science Foundation of Hubei Province (2011CDB154).

Notes and references

1 J. Chmiola, *Science*, 2010, **328**, 480.
2 N. Du, H. Zhang, J. X. Yu, P. Wu, C. X. Zhai, Y. F. Xu, J. Z. Wang and D. Yang, *Chem. Mater.*, 2009, **21**, 5264.
3 (*a*) G. F. Ortiz, I. Hanzu, P. Lavela, J. Tirado, P. Knauth and T. Djenizian, *J. Mater. Chem.*, 2010, **20**, 4041; (*b*) Y. Qi, N. Du, H. Zhang, X. Fan, Y. Yang and D. R. Yang, *Nanoscale*, 2012, **4**, 991.
4 (*a*) M. M. Shaijumon, E. Perre, B. Daffos, P. Taberna, J. Tarascon and P. Simon, *Adv. Mater.*, 2010, **22**, 4978; (*b*) J. Liu, G. Z. Cao, Z. G. Yang, D. H. Wang, D. Dubois, X. D. Zhou, G. L. Graff, L. R. Pederson and J. G. Zhang, *ChemSusChem*, 2008, **1**, 676.
5 M. D. Flerschauer, J. Li and M. J. Brett, *J. Electrochem. Soc.*, 2009, **156**, A33.
6 (*a*) J. Jiang, Y. Y. Li, J. P. Liu and X. T. Huang, *Nanoscale*, 2011, **3**, 45; (*b*) L. Li and N. Koshizaki, *J. Mater. Chem.*, 2010, **20**, 2972.
7 J. S. Chen, T. Zhu, X. H. Yang, H. G. Yang and X. W. Lou, *J. Am. Chem. Soc.*, 2010, **132**, 13162.
8 Y. G. Guo, J. S. Hu and L. J. Wan, *Adv. Mater.*, 2008, **20**, 2878.
9 (*a*) M. S. Park, G. X. Wang, Y. M. Kang, D. Wexler, S. X. Dou and H. K. Liu, *Angew. Chem., Int. Ed.*, 2007, **46**, 750; (*b*) Y. Wang, H. C. Zeng and J. Y. Lee, *Adv. Mater.*, 2006, **18**, 645; (*c*) X. Y. Xue, Z. H. Chen, L. L. Xing, S. Yuan and Y. J. Chen, *Chem. Commun.*, 2011, **47**, 5205.
10 J. Z. Wang, N. Du, H. Zhang, J. X. Yu and D. R. Yang, *J. Phys. Chem. C*, 2011, **115**, 11302.
11 W. W. Zhou, C. W. Cheng, J. P. Liu, Y. Y. Tay, J. Jiang, X. T. Jia, J. X. Zhang, H. Gong, H. H. Hng, T. Yu and H. J. Fan, *Adv. Funct. Mater.*, 2011, **21**, 2439.
12 (*a*) C. Li, W. Wei, S. M. Fang, H. X. Wang, Y. Zhang, Y. H. Gui and R. F. Chen, *J. Power Sources*, 2010, **195**, 2939; (*b*) J. X. Zhu, Z. Y. Lu, M. O. Oo, H. H. Hng, J. Ma, H. Zhang and Q. Y. Yan, *J. Mater. Chem.*, 2011, **21**, 12770.
13 J. S. Chen, D. Luan, C. M. Li, F. Y. C. Boey, S. Z. Qiao and X. W. Lou, *Chem. Commun.*, 2010, **46**, 8252.
14 J. Sarradin, M. Ribes, A. Guessous and K. Elkacemi, *Solid State Ionics*, 1998, **112**, 35–40.
15 G. F. Ortiz, I. Hanzu, P. Lavela, P. Knauth, J. L. Tirado and T. Djeniziana, *Chem. Mater.*, 2010, **22**, 1926.
16 J. P. Liu, X. T. Huang, Y. Y. Li, X. X. Ji, Z. K. Li, X. He and F. L. Sun, *J. Phys. Chem. C*, 2007, **111**, 4990.
17 J. P. Liu, Y. Y. Li, R. M. Ding, J. Jiang, Y. Y. Hu, X. X. Ji, Q. B. Chi, Z. H. Zhu and X. T. Huang, *J. Phys. Chem. C*, 2009, **113**, 5336.
18 J. P. Liu, Y. Y. Li, H. J. Fan, Z. H. Zhu, J. Jiang, R. M. Ding, Y. Y. Hu and X. T. Huang, *Chem. Mater.*, 2010, **22**, 212.
19 M. V. Reddy, T. Yu, C. H. Sow, Z. X. Shen, C. T. Lim, G. V. Subba Rao and B. V. R. Chowdari, *Adv. Funct. Mater.*, 2007, **17**, 2792.
20 J. P. Liu, Y. Y. Li, X. T. Huang, R. M. Ding, Y. Y. Hu, J. Jiang and L. Liao, *J. Mater. Chem.*, 2009, **19**, 1859.
21 J. Chen, L. Xu, W. Li and X. Gou, *Adv. Mater.*, 2005, **17**, 582.
22 C. Wu, P. Yin, X. Zhu, C. OuYang and Y. Xie, *J. Phys. Chem. B*, 2006, **110**, 17806.
23 H. Kim and J. Cho, *J. Mater. Chem.*, 2008, **18**, 771–775.
24 Y. Q. Song, S. S. Qin, Y. W. Zhang, W. Q. Gao and J. P. Liu, *J. Phys. Chem. C*, 2010, **114**, 21158.
25 Y. Wang, F. Su, J. Y. Lee and X. S. Zhao, *Chem. Mater.*, 2006, **18**, 1347.
26 X. L. Wu, Y. G. Guo, L. J. Wan and C. W. Hu, *J. Phys. Chem. C*, 2008, **112**, 16824.
27 Y. NuLi, P. Zhang, Z. P. Guo and H. K. Liu, *J. Electrochem. Soc.*, 2008, **155**, A196.
28 K. T. Nam, D.-W. Kim, P. J. Yoo, C.-Y. Chiang, N. Meethong, P. T. Hammond, Y.-M. Chiang and A. M. Belcher, *Science*, 2006, **312**, 885.
29 C.-L. Li, Q. Sun, G.-Y. Jiang, Z.-W. Fu and B.-M. Wang, *J. Phys. Chem. C*, 2008, **112**, 13782.
30 S. Mitra, P. Poizot, A. Finke and J. M. Tarascon, *Adv. Funct. Mater.*, 2006, **16**, 2281.
31 G. F. Ortiz, I. Hanzu, P. Lavela, J. L. Tirado, P. Knauth and T. Djenizian, *J. Mater. Chem.*, 2010, **20**, 4041.
32 J. S. Chen, C. M. Li, W. W. Zhou, Q. Y. Yan, L. A. Archer and X. W. Lou, *Nanoscale*, 2009, **1**, 280.